Geophysical Research Letters

RESEARCH LETTER
10.1029/2022GL100209

Key Points:

- Effective porosity was derived from cation exchange capacity analysis on samples from Site C0002, the deepest International Ocean Discovery Program borehole ever drilled
- Total and effective porosities decay exponentially all along Site C0002, down to the heart of the Nankai accretionary prism (3,000 mbsf)
- Modifying the parameters of the Erickson-Jarrard model using effective porosity and clay content improves the *P*-wave velocity prediction

Supporting Information:

Supporting Information may be found in the online version of this article.

Correspondence to:

M.-L. Doan,
Mai-linh.doan@univ-grenoble-alpes.fr

Citation:

Doan, M.-L., Dutilleul, J., & Henry, P. (2023). Effective porosity profile at IODP Site C0002 in the heart of the Nankai accretionary prism, and its use for predicting in situ seismic velocities. *Geophysical Research Letters*, *50*, e2022GL100209. https://doi.org/10.1029/2022GL100209

Received 1 JUL 2022
Accepted 26 DEC 2022

Author Contributions:

Conceptualization: Mai-Linh Doan
Data curation: Mai-Linh Doan, Jade Dutilleul
Investigation: Mai-Linh Doan, Jade Dutilleul, Pierre Henry
Methodology: Mai-Linh Doan, Jade Dutilleul, Pierre Henry
Resources: Mai-Linh Doan, Jade Dutilleul, Pierre Henry
Software: Mai-Linh Doan
Supervision: Mai-Linh Doan

Effective Porosity Profile at IODP Site C0002 in the Heart of the Nankai Accretionary Prism, and Its Use for Predicting In Situ Seismic Velocities

Mai-Linh Doan[1], Jade Dutilleul[2], and Pierre Henry[3]

[1]Univ. Grenoble Alpes, Univ. Savoie Mont Blanc, CNRS, IRD, Univ. Gustave Eiffel, ISTerre, Grenoble, France, [2]Univ. Lorraine, CNRS, GeoRessources, Nancy, France, [3]Univ. Aix-Marseille, CNRS, IRD, INRAE, Coll France, CEREGE, Aix-en-Provence, France

Abstract Using logging data and samples collected by the four expeditions of the International Ocean Discovery Program NanTroSEIZE drilling campaign that occupied Site C0002 in the Nankai margin located southwest of Japan, we determined effective porosity and sonic velocity profiles down to 3 km below the seafloor in the accretionary prism, above the seismogenic plate interface. We measured cation exchange capacity to differentiate clay-bound water content from effective porosity, which is representative of compaction. The decrease in effective porosity with depth is fitted with a single exponential decay, which suggests hydrostatic conditions for most of the borehole. The Erickson-Jarrard template was adapted to account for the actual clay-bearing nature of the sediments. We used this improved *P*-wave velocity–effective porosity relationship to fill shipboard data gaps and predict *P*- and *S*-wave velocity profiles at Site C0002.

Plain Language Summary Effective porosity reflects the network of pores that affects the transport properties and the history of sediment compaction. However, evaluating this property is not straightforward given that standard methods provide total porosity, which also includes clay-bound water. We can estimate the effective porosity using cation exchange capacity of the rocks. This method was used at Site C0002, the deepest hole in history of the International Ocean Discovery Program, drilled down to the heart of the Nankai accretionary prism, located southwest of Japan. We show that the effective porosity follows a simple exponential decay law with depth. We also demonstrate that there is a single relationship between effective porosity and *P*-wave velocity. We use this relationship to fill the data gaps in the *P*- and *S*-wave velocity profiles at Site C0002. Conversely, this provides a direct method to estimate effective porosity, and hence, the compaction state, from seismic profiles acquired across the Nankai accretionary prism.

1. Introduction

The Nankai Trough Seismogenic Zone Experiment (NanTroSEIZE) is an ambitious initiative to investigate fault processes and mechanisms of earthquake and tsunami generation at active plate boundary systems. The program focused on the Kumano transect of the Nankai subduction zone, offshore southwest Japan. Since 2007, 11 expeditions of the Integrated Ocean Drilling Program and later International Ocean Discovery Program have explored various parts of the accretionary prism, providing geological samples and *in situ* measurements recorded by logging and/or borehole monitoring.

The main site of NanTroSEIZE was Site C0002 at ~35 km from the trench of the Nankai subduction zone in the Kumano forearc basin, above a portion of the plate interface believed to be capable of seismogenic locking and slip. This portion of the megathrust is branched by a megasplay system of faults. It also coincides with the updip limit of the coseismic rupture zone of the 1944 Tonankai earthquake (Park et al., 2002). Slow slip events, very low frequency earthquakes, and tectonic tremors have also been identified nearby (Araki et al., 2017; Obara & Kato, 2016). Drilling operations at Site C0002 were designed to characterize the compositional, petrophysical, mechanical, and hydrogeological properties of the accretionary wedge with a series of holes penetrating the Kumano forearc basin and accretionary sediments beneath. Ultimately, Site C0002 aimed to unravel the roles of the plate boundary and the system of megasplay faults in accommodating plate motion, by reaching a drilling target of 5 kilometers below seafloor (kmbsf; below 2 km of seawater) where seismogenic conditions are thought to be present. Although technical issues prevented the completion of this objective, the holes drilled at Site C0002 during the final NanTroSEIZE expedition reached 3 kmbsf providing an unprecedented record of *in*

Validation: Mai-Linh Doan, Pierre Henry
Visualization: Jade Dutilleul
Writing – original draft: Mai-Linh Doan, Jade Dutilleul
Writing – review & editing: Mai-Linh Doan, Jade Dutilleul

situ data and collection of samples within an accretionary wedge. Still, Site C0002 provides first-hand data at the middle of the Nankai accretionary prism.

Hydrologic models require accurate compaction profile as inputs. To do so, pore pressure or P to S wave velocity ratio (V_p/V_s) are needed. However, getting reliable estimates of these parameters at depth is difficult and can only be achieved with scientific drilling.

The objective of this study is twofold: (a) obtain an effective porosity profile from analysis of cores, and (b) improve the V_p prediction from porosity to get complete V_p and V_s profiles and predict missing data down to ∼3 kmbsf at Site C0002. We use logging data and samples collected by the four expeditions that occupied Site C0002 to determine the compaction and sonic velocity profiles. It has been shown that in clay-rich sediments such as those drilled at Site C0002, the water structurally bound to the clay particles affects the porosity measurements, resulting in biased porosity–velocity relationships (Brown & Ransom, 1996; Tudge & Tobin, 2013). Here, we measure cation exchange capacity (CEC) on core samples to differentiate the clay-bound water content from the effective porosity (representative of the compaction state of the sediments) from the total porosity routinely measured during the cruises (Conin et al., 2012; Dutilleul, Bourlange, Conin, et al., 2020; Dutilleul, Bourlange, & Géraud, 2021; Dutilleul, Bourlange, Géraud, et al., 2020, 2021; Henry, 1997; Henry & Bourlange, 2004). Then, we propose a modified version of the Erickson-Jarrard model (Erickson & Jarrard, 1998) fitting better the V_p–porosity crossplot using effective porosity and shipboard mineralogical data. This allows us to provide sonic velocity profiles at Site C0002. The improved relationship between V_p and effective porosity can ultimately be used to derive the compaction state and hydrological properties in the Nankai accretionary prism.

2. Materials

In this study, we synthesize sample and logging data collected by the four expeditions that occupied Site C0002 to identify data gaps. We also provide new data (CEC, effective porosity, pore size distribution, and permeability).

2.1. Sampled Intervals and Lithology

Repeated drilling efforts at Site C0002 have resulted in the collection of cores and cuttings in the lower Kumano forearc basin and in the inner wedge of the Nankai accretionary margin, down to ∼3,263 mbsf (Figure 1a). In 2007, Expedition 315 retrieved 86 cores mainly from the Kumano forearc basin: from the seafloor to ∼204 mbsf in Holes C0002C and C0002D and from ∼475 to 1,057 mbsf in Hole C0002B (Kinoshita et al., 2009a). In 2012, Expedition 338 drilled Hole C0002F and penetrated the upper part of the accretionary prism providing cuttings from ∼860 to 2,005 mbsf (Strasser et al., 2014). Furthermore, 44 cores were collected from ∼200 to 503 mbsf (Holes C0002K and C0002L), ∼902 to 934 mbsf (Hole C0002J), and ∼1,100 to 1,112 mbsf (Hole C0002H). Approximately 1 year later, the accretionary prism was further sampled down to ∼3,059 mbsf during Expedition 348, with cuttings retrieved in Holes C0002N and C0002P (Tobin et al., 2015). Limited coring was conducted between ∼2,163 and ∼2,219 mbsf in Hole C0002P and between ∼475 and ∼513 mbsf in Hole C0002M. Finally, in 2018–2019, sampling reached ∼3,263 mbsf with 240 cutting samples collected in Holes C0002Q–C0002T during Expedition 358 (Kitajima et al., 2020). Also, the ∼2,836–2,846 mbsf interval was cored in Hole C0002T, providing the three deepest cores ever drilled in IODP history.

Based on these samples, the shipboard scientists (Kinoshita et al., 2009b; Kitajima et al., 2020; Strasser et al., 2014; Tobin et al., 2015) defined lithological Units I–III in the Kumano forearc basin sediments and IV–V in the upper accretionary prism sediments (Figure 1b). Units I (0 to ∼136 mbsf in Hole C0002D) and II (∼136–826 mbsf in Holes C0002B, C0002D, C0002K, and C0002L) correspond to Quaternary-aged basin-plain facies with alternating dark greenish to grayish hemipelagic silty clay to clayey silt, and silty-grained turbidites (Kinoshita et al., 2009b). In addition, Unit I includes many volcanic ash layers. Unit III (between ∼834 and 922–1,025 mbsf in Holes C0002B, C0002F, and C0002J) is greenish, grayish, or brownish silty claystone representing basal forearc basin facies of the Pleistocene to Late Miocene (Kinoshita et al., 2009b; Strasser et al., 2014). Accretionary prism Unit IV (between ∼922–1,025 mbsf and ∼1,740 mbsf in Holes C0002B, C0002F, and C0002N) is greenish gray silty claystone. Sandstone content increases with depth up to ∼60%, allowing the shipboard identification of five subunits (IVA–IVE; Kitajima et al., 2020; Strasser et al., 2014; Tobin et al., 2015). Unit V, drilled down to ∼3,263 mbsf in Holes C0002F, C0002N, and C0002P–C0002T, is mainly composed of greenish gray silty claystone and fine silty claystone, with minor to moderate sandstone (Kitajima et al., 2020; Tobin et al., 2015).

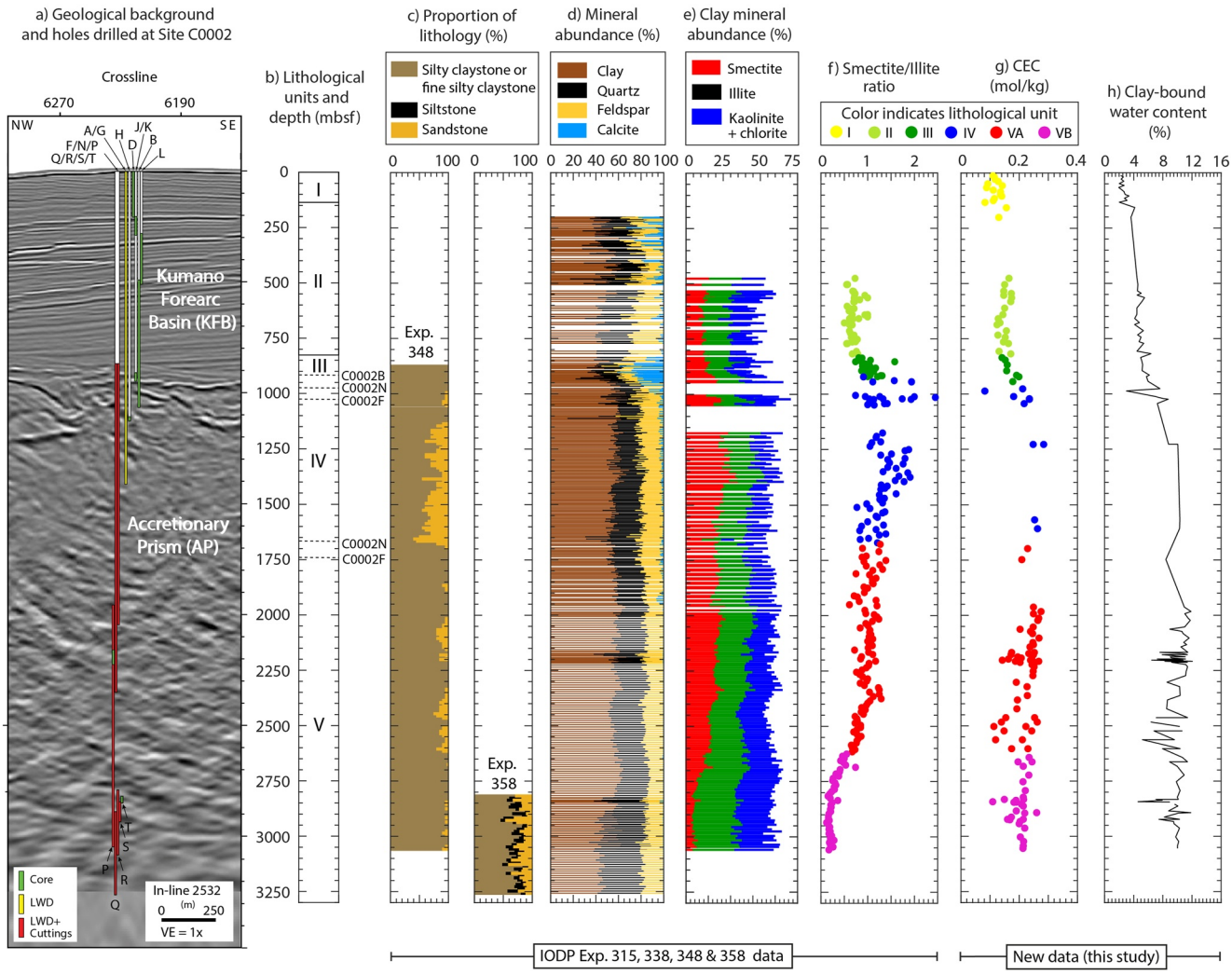

Figure 1. Summary of lithological and mineralogical data at Site C0002, including shipboard and postcruise analyses used in this study (a–f; Guo & Underwood, 2012; Kinoshita et al., 2009a; Strasser et al., 2014; Tobin et al., 2015, 2020; Underwood, 2017; Underwood & Song, 2016) and new data (g, h). (a) Seismic image along with depth ranges over which LWD, coring, and cuttings were acquired at Site C0002. (b) Lithological units. (c) Lithological proportions. (d) Bulk mineral composition from X-ray diffraction analysis (XRD). (e) Clay mineralogy from XRD. (f) Smectite/illite ratio. (g) Cation exchange capacity (CEC) and (h) clay-bound water content of the samples.

2.2. Porosity Data

The four expeditions that occupied Site C0002 recovered over 900 core samples and 350 hand-picked intact cuttings to conduct moisture and density (MAD) analyses following the procedure of Blum (1997), providing total porosity and grain density. To conduct CEC measurements and determine effective porosity, we collected 87 samples in combination with MAD samples from Expeditions 338, 348, and 358. We reuse the 48 CEC data from Conin et al. (2012) for the 0–1 kmbsf depth interval drilled during Expedition 315. We also determine the porosity and pore size distribution of one core sample from Hole C0002T (2.8 kmbsf) to extend the study of Dugan (2015) restricted to 2 kmbsf (Figure 2c).

2.3. Sonic Data

In situ sonic data at Site C0002 were acquired using Logging While Drilling. The tools used were Schlumberger SonicVision in Holes C0002A and C0002F, the Halliburton XBAT in Hole C0002P, and the Schlumberger Sonic-Scope in Hole C0002S. In total, V_p was measured almost continuously down to 3,058.4 mbsf, with a gap in data between 1,986.5 and 2,250.4 mbsf (Figure 2d). Although various attempts have been made, *S* wave velocity

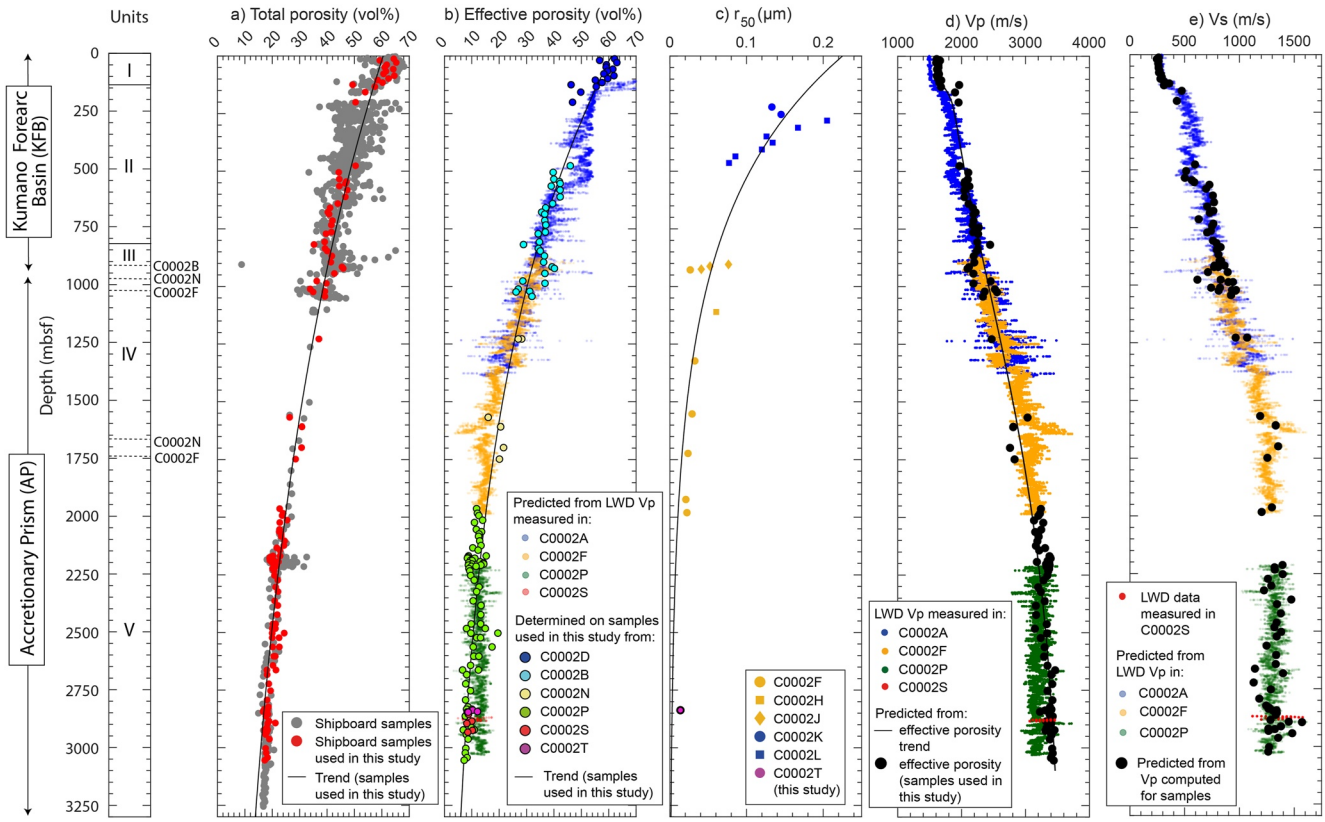

Figure 2. Compilation of porosity (a, b), pore size (c), and sonic (d, e) data at Site C0002. In (b) and (e), predictions are shown in dull colors, in contrast to LWD and sample data. In (c), data from Holes C0002F–C0002L are from Dugan (2015).

(V_s) was reliably measured only at a discrete location ~2,880 ± 3.5 mbsf in the lower section of Hole C0002S (Figure 2e). The V_s data in Hole C0002P were of too poor quality to be usable. During Expedition 358, difficult side-tracking from Hole C0002P precluded measurement of V_s in Holes C0002Q, C0002R, and C0002T. Furthermore, repeated drilling runs damaged the upper section of C0002S, resulting in inconsistent sonic velocities. V_p and V_s are reliable only between 2,877 and 2,884 mbsf, where V_p values are in the same range as in C0002P, suggesting an intact section (Kitajima et al., 2020).

3. Methods

Our workflow involves four steps:

1. We measure CEC on samples from which we determine the effective porosity trend.
2. We determine an empirical fit linking V_p and effective porosity to satisfactorily predict V_p.
3. We use this relationship to interpolate V_p and fill the gaps in the V_p data set. Reciprocally, we also predict missing effective porosity values from LWD V_p.
4. We predict missing V_s data from the V_p data.

3.1. Porosity Characterization From Core Samples

Effective porosity ϕ_{eff} was determined on 135 core samples and hand-picked intact cuttings based on the total porosity (ϕ_t) and grain density (ρ_s) determined during the cruises, the CEC (mol/kg), the average number of water molecules per cation charge (n = 12 following Henry and Bourlange [2004] and Conin et al. [2012]), and the water molar mass (m_w = 0.018 kg/mol) and density (ρ_w = 1,024 kg/m^3):

$$\phi_{\text{eff}} = \phi_t - n\,\frac{m_w}{\rho_w}\,CEC\,\rho_s\,(1-\phi_t) \quad (1)$$

CEC was determined by exchange with cobaltihexamine (Orsini & Rémy, 1976), following standard NF X31-130. Standard error is 1.5% on all determinations. The CEC of the samples collected during IODP Expeditions 338 and 348 was determined at the INRA soil analysis laboratory in Arras, France. The CEC of the samples retrieved during IODP Expedition 358 was measured at the LIEC laboratory in Metz, France.

To further document effective porosity and estimate permeability, we conducted mercury injection experiment using a Micromeritics AutoPore IV 9500 at GeoRessources, in Nancy, France, on a core catcher sample from core C0002T-1K collected at ~2,837 mbsf during IODP Expedition 358. The experimental procedure and the permeability model of Katz and Thompson (1986, 1987) are detailed in Supporting Information S1.

3.2. Prediction of *P* Wave Velocity From Porosity

The empirical model of Erickson and Jarrard (1998) is widely used to predict *P* wave velocities (V_p) of the sediments of the Nankai accretionary prism (Kitajima et al., 2017; Kitamura et al., 2021) or its input sediments (Hoffman & Tobin, 2004; Tudge & Tobin, 2013). The model acknowledges the effect of porosity and shale content for sediments showing normal or high consolidation. Following Jeppson and Kitajima (2022), we use a generic formulation of this model (Equations 2 and 3, referred hereafter to as the Erickson-Jarrard template, which will be further extended to apply to the model of Tudge and Tobin [2013]):

$$V_p = A + B\phi + \frac{H}{(\phi + C)^2 + D} + E\,(V_{sh} - F)\,X_m \tag{2}$$

where ϕ is porosity (either total porosity ϕ_t or effective porosity ϕ_{eff}), V_{sh} is the shale volume, *A*–*H* are empirical constants, and X_m accounts for the abrupt change in behavior at a critical porosity ϕ_c, above which stress is supported by the fluid rather than by the grain skeleton of the rock (Equation 3):

$$X_m = \tanh[G(\phi - \phi_c)] - \|\tanh[G(\phi - \phi_c)]\| \tag{3}$$

where G is an empirical constant. In the initial paper by Erickson and Jarrard (1998), $G = 40$ for normally consolidated sediments and $G = 20$ for highly consolidated sediments. However, parametric study (see Supporting Information S1) shows that the V_p prediction is little dependent on this parameter. In most studies, except for Tudge and Tobin (2013), $H = 0.305$. When $\phi_t = 1$, then by construction $X_m = 0$ and $V_p = A + B + \frac{H}{(1+C)^2+D}$. As at $\phi_t = 1$, $V_p = V_{water}$, this constrains D as a function of A, B, and C. When $\phi_t = 0$, $X_m = -2\tanh[G\phi_c] \sim -2$, and $V_p = A + \frac{H}{C^2+D} - 2E\,(V_{sh} - F)$. Therefore, for pure sandstone matrix ($\phi = 0$, $V_{sh} = 0$), $V_{p,sandstone}[\text{km/s}] = A + \frac{H}{C^2+D} + 2EF$, while for pure shale matrix ($\phi = 0$, $V_{sh} = 1$), $V_{p,clay}[\text{km/s}] = A + \frac{H}{C^2+D} - 2E(1 - F)$.

Table 1 reports the parameters used in previous studies to fit the empirical data with the Erickson-Jarrard template, all based on total porosity. In this study, we propose a new inversion of the Erickson-Jarrard template on the C0002 data set for both total and effective porosities. The inversion was operated with the `optimize` module of the Python `SciPy` package, using the parameters of Kitamura et al. (2021) as initial parameters and a L^2 cost function, using the classical Euclidian norm. Quality of the fit was estimated via residual standard errors (RSEs).

3.3. Determination of the *S* Wave Velocity Profile

The four IODP expeditions that occupied Site C0002 only provided a single V_s value, at ~2,880 ± 3.5 mbsf. Therefore, we rely on theory to estimate the profile of V_s along the 3-km-section drilled at Site C0002.

The bulk (K) and shear (μ) modulus of the fluid-saturated rock are related to the *P* and *S* wave velocities.

$$V_p = \sqrt{\frac{K + \frac{4}{3}\mu}{\rho}} \qquad V_s = \sqrt{\frac{\mu}{\rho}} \tag{4}$$

The bulk density of the rock ρ can be computed from the grain density $\rho_s = 2{,}700$ kg/m^3 and the total porosity, provided by MAD measurements onboard. Hence, the knowledge of V_p and V_s at 2,880 ± 3.5 mbsf provides K and μ.

Geophysical Research Letters

10.1029/2022GL100209

Table 1
Parameters Used in the Empirical Model of Equation 2, for This and Several Previous Studies Focusing on the Nankai Margin

	Coefficients of the Erickson-Jarrard template										Matrix V_p (m/s)				Matrix V_s (m/s)		
Study	V_{sh}	ϕ_c	A	B	C	D	E	F	G	H	Water ($\phi = 1$)	Matrix ($\phi = 0$)	Pure sand ($\phi = 0$, $V_{sh} = 0$)	Pure shale ($\phi = 0$, $V_{sh} = 1$)	Nankai matrix ($\phi = 0$)	Pure sand ($\phi = 0$, $V_{sh} = 0$)	Pure shale ($\phi = 0$, $V_{sh} = 1$)
Tudge and Tobin (2013)	0.75	0.20	1.592	−0.203	0.300	0.0715	0.57	2.505	10.90	0.195	1,500	4,750	5,583	4,472	2,278	2,781	2,113
Erickson and Jarrard (1998) adapted by Kitajima et al. (2017)	0.66	0.39	1.11	0.178	0.135	0.0775	0.61	1	20	0.305	1,510	4,711	5,516	4,296	2,255	2,741	2,010
Hoffman and Tobin (2004)	1.057	0.295	0.746	0.532	0.124	0.05131[a]	0.61	1.13	40	0.305	1,510	5,402	6,692	5,472	2,671	3,459	2,714
Kitamura et al. (2021)	0.90	0.4605	0.6933	0.5523	0.0409	0.0701[a]	0.61	1.123	40	0.305	1,510	5,215	6,312	5,093	2,558	3,227	2,484
This study: *E–G* based on previous studies (total porosity)	0.905	0.56	0.6803	0.5670	0.0416	0.0761[a]	0.61	1.123	40	0.305	1,510	4,866	5,970	4,750	2,347	3,018	2,278
This study: *E–G* based on previous studies (effective porosity)	1.003	0.55	0.6940	0.5560	0.0319	0.1082[a]	0.61	1.123	40	0.305	1,510	3,631	4,855	3,635	1,667	1,780	1,669
This study: V_{sh} based on mineralogy (total porosity)	**0.60**	0.56	0.6803	0.5670	0.0416	0.0761[a]	**0.254**	1.123	40	0.305	1,510	4,865	5,170	4,662	2,347	2,531	2,225
This study: V_{sh} based on mineralogy (effective porosity)	**0.60**	0.55	0.6940	0.5560	0.0319	0.1082[a]	**0.140**	1.123	40	0.305	1,510	3,631	3,799	3,520	1,667	2,644	1,669

Note. These parameters were used to draw the empirical models of Figure 3.
[a]$D = H/(V_p(water, [km/s]) - A - B) - C^2 - 2C - 1$.

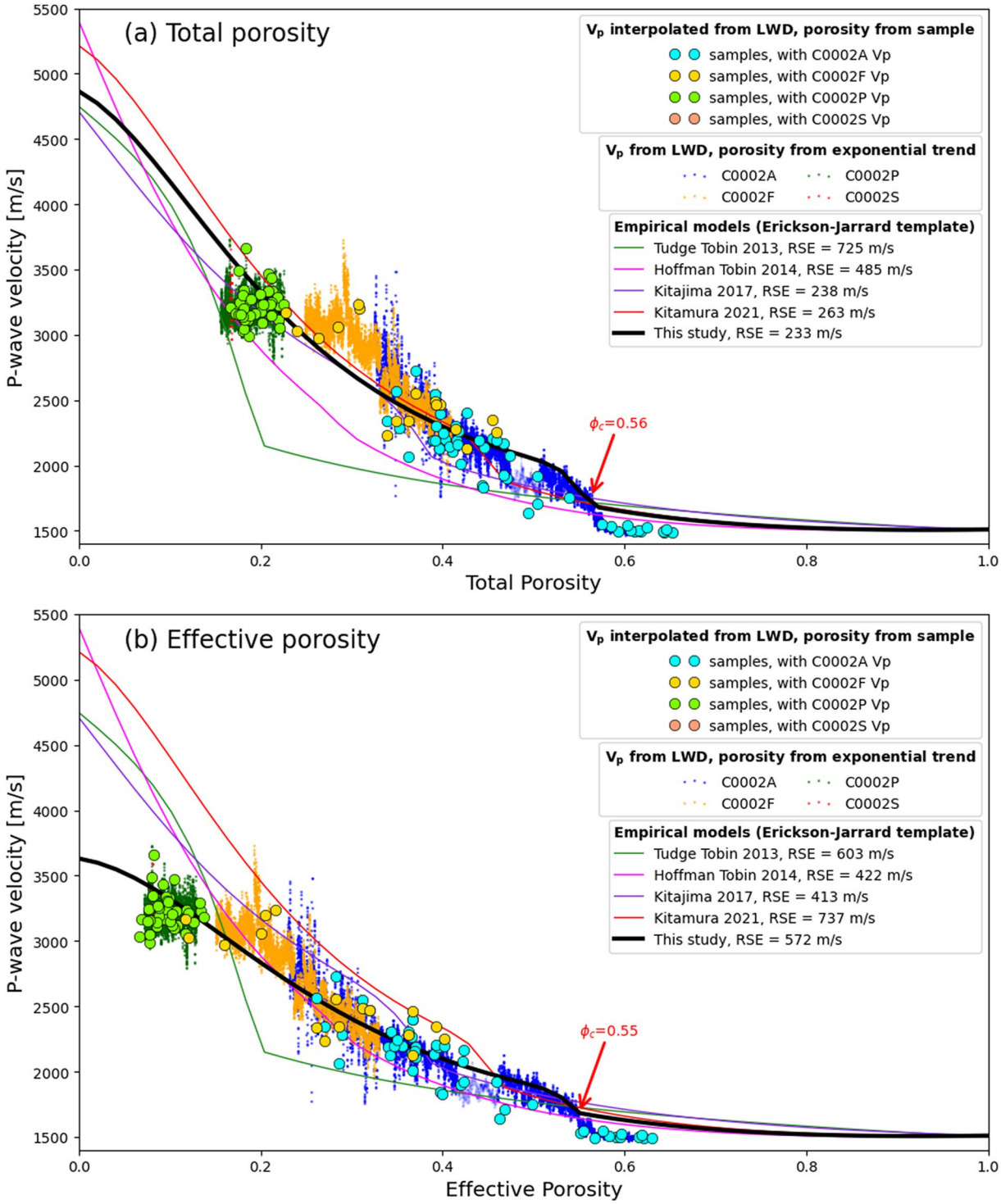

Figure 3. Crossplot between *P* wave velocity and (a) total porosity, and (b) effective porosity. Crossplots can be built either from the sample data for which the *P* wave velocity of logs are interpolated (large circled colored points), or from the LWD data for which the corresponding porosity has been derived from the exponential trend of Equation 7. The empirical models of Erickson and Jarrard (1998) (modified by Kitajima et al., 2017), Hoffman and Tobin (2004), and Kitamura et al. (2021) are also reported. A new inversion fit is also proposed (thick black line), based on Equation 2, with the coefficients of Table 1.

At that depth, the effective porosity is $\phi_{\text{eff}} = 0.08$. The Gassmann equation allows to estimate both sonic velocities through the bulk modulus (K in Pa) and shear modulus (μ in Pa) of the fluid-saturated rock:

$$\frac{K}{K_s - K} = \frac{K_{dry}}{K_s - K_{dry}} + \frac{K_f}{\phi_{\text{eff}}(K_s - K_f)} \qquad \mu = \mu_{dry} \tag{5}$$

where K_{dry} and μ_{dry} are the bulk and shear modulus, respectively, for the dry material, filled with very compressible fluid. K_s and μ_s are the bulk and shear modulus of the grain material composing the skeleton of the rock. K_f is the incompressibility modulus of the fluid and set to 2 GPa.

Equation 5 provide only two equations for four unknowns in the equations: K_{dry}, μ_{dry}, K_s, and μ_s and more assumptions are needed. The extrapolation of the Erickson-Jarrard template to $\phi_{\text{eff}} = 0$ provides the P wave velocity of the matrix $V_{p,s} = \sqrt{\frac{K_s + \frac{4}{3}\mu_s}{\rho_s}}$ and an additional relation.

Also, we assume (Brie et al., 1995; Doan et al., 2011)

$$\frac{K_{dry}}{\mu_{dry}} = \frac{K_s}{\mu_s} \tag{6}$$

First, by combining Equations 6 and 5, a second-order polynomial equation allows to determine K_s. Equation 6 then provides μ_s. Second, the Gassmann equations allow to compute K and μ (hence V_p and V_s for all porosities and fluids). Full details of the algorithm are provided as Supporting Information S1.

Once the grain parameters for the matrix are estimated, the two unknowns K and μ can be computed from Equations 6 and 5 for every effective porosity ϕ_{eff}. The full algorithm is given in Supporting Information S1. As K is also provided by Equation 2, the shear velocity μ is constrained.

4. Results

4.1. Evolution of Cation Exchange Capacity

CEC values measured at Site C0002 are low in the Kumano forearc basin (~0.16 mol/kg on average) and moderate (~0.22 mol/kg on average) in the upper accretionary prism (Figure 1g). The low CEC values in the Kumano forearc basin are associated with a moderate total clay content (~46%), consisting of minor smectite (~13%) and illite (~19%). Unit III marks the transition toward higher CEC values, with a maximum of 0.28 mol/kg reached at ~1,250 mbsf (Subunit IVC) in the upper accretionary prism which is characterized by higher total clay (~58%) and smectite (~25%) contents. In Subunit VA, illite and kaolinite/chlorite become the dominant clay minerals, reaching ~33% and ~25% of samples bulk composition, respectively, whereas smectite content quickly depletes to ~5%. However, the drop in the smectite/illite ratio in Subunit VB inferred from X-ray diffraction analysis (XRD) data accounts for a moderate variation in CEC.

4.2. Effective Porosity Profile

Total porosity decreases from ~65% at the seafloor to ~16% in the heart of the accretionary prism ~3,250 mbsf (Figure 2a). Clay-bound water content increases from 2% to 7% with depth in the Kumano forearc basin and shows scattered values ranging 4%–12% (~10% on average) in the upper accretionary prism Units IV and V. As a consequence of both total porosity and clay-bound water profiles, the effective porosity decreases from ~62% at the seafloor to ~8% at the bottom of Site C0002 ~3,000 mbsf (Figure 2b). Both the total and effective porosities can be fitted by an exponential law:

$$\phi = \phi_0 e^{-\alpha z} = \phi_0 e^{-\frac{z}{L}} \tag{7}$$

where ϕ_0 and L are empirical constants and z is the depth. Here, $\phi_0 = 61.0\%$ and $L = 1{,}421.6$ m for the effective porosity ($R^2 = 0.97$), and $\phi_0 = 60.5\%$ and $L = 2{,}234.6$ m ($R^2 = 0.97$) for the total porosity.

4.3. Evolution of Pore Size Distribution

The sample analyzed by mercury injection from Hole C0002R (2,837 mbsf) shows a dominant family of pores with radius ~0.014 μm (Figure 2c). Similarly to effective porosity, this value can be fitted with the values obtained by Dugan (2015) for shallower samples from the forearc basin, using an exponential decay trend (Equation 8):

$$r = r_0\, e^{-\alpha z} = r_0\, e^{-\frac{z}{L}} \tag{8}$$

with $r_0 = 0.23$ μm and $L = 650$ m ($R^2 = 0.85$).

The Katz-Thompson permeability (Katz & Thompson, 1986, 1987) of the sample from Hole C0002R is $\sim 3 \times 10^{-19}$ m^2, which is 2 orders of magnitude lower than reported by Song and Underwood (2017) at ~2,200 mbsf based on constant-flow permeability tests.

4.4. Relationship Between Porosity and Sonic Velocities

Despite the variety of geophysical tools used and the 12-year interval between the first and last data acquired, all sonic data are consistent (Figure 2). V_p starts from 1,500 m/s in the shallow high-porosity sediments and tends to increase exponentially with depth leveling at 3,150 m/s in the bottom Unit V. However, two anomalous zones can be identified. In the Kumano forearc basin, a low V_p zone is associated with a Bottom Seismic Reflector (BSR) at 400 mbsf (Bangs et al., 2010; Miyakawa et al., 2014) and with a turbiditic zone saturated with free gas extending down to 547 mbsf below (Chhun et al., 2018; Saito et al., 2010). Sonic anomalies related to gas hydrates have been modeled to extend over several hundreds of meters (Westbrook et al., 2008). In the upper accretionary prism, V_p peaks to 3,700 m/s at 1,600 m (Figure 2c) in a quartz-rich sand interval (Figure 1d) where a positive peak in resistivity occurs (Strasser et al., 2014).

We show a crossplot of V_p versus porosity, considering either total or effective porosity (Figure 3). Given that the logging data and the samples on which porosity was measured do not have the same sample depth base, two options are possible to make the crossplot. The first one is to interpolate the V_p at each sample depth from LWD data for each log. The second one is to interpolate the porosity for each LWD depth using the exponential decay trend of Equation 7. The first option provided less data, but the interpolation was recovered from the denser LWD data that better caught the heterogeneity along the borehole. Based on the Erickson-Jarrard template (Equations 2 and 3), the best fit data inversion is obtained with the coefficients reported in the two last lines of Table 1. The resulting fitting curves are shown in Figure 3 as thick black lines.

The S wave velocity profile derived from the data acquired at ~2,880 ± 3.5 mbsf increases exponentially with depth, starting from ~290 m/s in the shallow high-porosity sediments of the Kumano forearc basin to ~1,400 m/s in the heart of the accretionary prism ~3,000 mbsf (Figure 2e).

5. Discussion and Conclusion

5.1. A Single Compaction Curve at Site C0002

So far, most studies aiming to characterize the compaction state of accretionary wedges have been using total porosity data (Hunze & Wonik, 2007; Kitajima et al., 2017; Kominz et al., 2011; Raimbourg et al., 2011; Saito & Goldberg, 1997) to interpret anomalies (i.e., departure of porosity data from the vertical loading exponential decay) in terms of tectonic or hydrologic events (e.g., anomalously high porosity may indicate undercompaction due to excess pore pressure build-up in poorly drained conditions). Only a few attempts have been made based on effective porosity. These attempts have focused on the input sedimentary sections (Dutilleul, Bourlange, Conin, et al., 2020; Dutilleul, Bourlange, Géraud, et al., 2020; Henry & Bourlange, 2004) or shallow accreted sections (<1 kmbsf; Conin et al., 2012; Dutilleul, Bourlange, & Géraud, 2021; Henry & Bourlange, 2004).

Determining effective porosity from 0 to ~3,250 mbsf at Site C0002 in the Nankai margin, we provide the longest effective porosity profile (effective porosity trend in Figure 2b) ever obtained at subduction zones. Effective porosity follows a single normal compaction curve over the entire drilled section.

Similarly, along other wells drilled in other subduction zones, either on splay faults (Conin et al., 2012; Dutilleul, Bourlange, & Géraud, 2021) or at the decollement (Hunze & Wonik, 2007; Saito & Goldberg, 1997), a single

compaction curve could describe the porosity of hanging walls formed by siliciclastic clay-rich sediments. Beneath, in the footwall, distinct compaction curves were commonly identified.

5.2. An Improved *P* Wave Velocity–Porosity Relationship, Consistent With Geological Data

5.2.1. The New Parameters Are More Respectful of Geology

Previous studies using the Erickson-Jarrard template used a wide range of parameters, sometimes not consistent with geological information (Table 1).

Following Nur et al. (1998), critical porosity is interpreted as the transition from fluid-supported medium to matrix-supported medium, where stress gets transmitted through the grain skeleton. For granular material, expected values are ∼0.3–0.4 (Erickson & Jarrard, 1998;Nur et al., 1998). In clay-rich sediments, the critical porosity should be higher as the grains to be considered are clay aggregates with internal porosity. In Figure 3, the critical porosity is expressed as a kink in the $V_p - \phi$ curve. Care should be taken not to use the data related to the BSR anomaly (corresponding to the translucent dots around 45% porosity in Figure 3). Hence, we determined $\phi_c \sim 56\%$, a higher value than for previous studies.

A second issue was the shale volume V_{sh}. It was initially derived from the gamma ray log used as a proxy for clay volume, resulting in very high values, sometimes ≥1 (Erickson & Jarrard, 1998; Hoffman & Tobin, 2004; Tudge & Tobin, 2013). Recent studies use lower V_{sh} values based on core data, such as the proportion of fine grains like clays and silts (Kitamura et al., 2021), or mineralogical data from XRD analyses (Jeppson & Kitajima, 2022).

A third issue was the type of porosity considered. Initially, total porosity values were used (Hoffman & Tobin, 2004; Kitajima et al., 2017; Kitamura et al., 2021). Recent studies have shown that because of the effect of clay-bound water on total porosity, better relationships with V_p can be obtained using effective porosity (Jeppson & Kitajima, 2022; Tudge & Tobin, 2013). In this study, if only total porosity was considered, the best fit option using the Erickson-Jarrard template (Equations 2 and 3) stays close to the solution of Kitamura et al. (2021) (RSE = 233 m/s), that tends to predict high V_p at low porosity. If effective porosity is considered instead, the new fit provides moderate V_p at low porosity, which better matches the observed trend (RSE = 159 m/s). In both cases, the best fit solutions suggest a clay content $V_{sh} \sim 0.905$ for total porosity and $V_{sh} \sim 1.003$ for effective porosity (Table 1). However, by definition, $0 \leq V_{sh} \leq 1$, and the mineralogical analyses suggest lower values (Figure 1d). Setting $V_{sh} = 60\%$ for consistency with shipboard XRD analyses, Equation 2 of the Erickson-Jarrard template implies to decrease E down to 0.254 for total porosity and to 0.14 for effective porosity to keep the factor $V_{sh} \times E$ constant (Table 1). A sensitivity study (Figures S4 and S5 in Supporting Information S1) shows this parameter E offsets the seismic velocity at lower porosity.

5.2.2. Consistency With Other Data Sets

Using a V_{sh} consistent with shipboard XRD analyses (Figure 1d) and the effective porosity instead of the total porosity (Figure 3), we account for the clay-rich content of the formation and the influence of the clay-bound water, which improves the quality of the V_p–porosity fit relative to previous studies.

The *P* wave velocity–porosity relationships determined in this study with total porosity and effective porosity predict lower V_p for Nankai matrix ($\phi = 0$), pure shale matrix, and pure sand matrix than classical estimates. In particular, the prediction based on effective porosity fits well the empirical estimate for the clay end-member of Tosaya (1982) and Castagna et al. (1985) (Figure S2 in Supporting Information S1). Bound water content contributes to the high compliance of this clay end-member.

The *P* wave velocity–effective porosity determined in this study for Site C0002 is also consistent with the V_p–effective porosity data compiled by Jeppson and Kitajima (2022) for sediment inputs to the Sunda (IODP Expedition 362 Site U1480) and North Hikurangi (IODP Expedition 372/375 Site U1520) margins showing diverse lithologies (Figure S3 in Supporting Information S1).

In summary, prescribing sensible values of V_{sh} and using the actual effective porosity, we retrieve V_p for pure shale more consistent with previous studies.

5.3. Implications for Hydromechanics at Site C0002

The effective porosity determined from samples shows no departure from the exponential compaction curve, which suggests a constant ratio between pore pressure and overburden stress (Athy, 1930). Given that borehole

observatory data show no overpressure down to ~1 kmbsf (Araki et al., 2017), the single compaction curve suggests that this constant ratio corresponds to hydrostatic conditions. This is consistent with regional seismic profiles (Chhun & Tsuji, 2021) which predict overpressure only much deeper in the accretionary prism, beneath the megasplay fault zone (Kitajima & Saffer, 2012; Park et al., 2010; Tsuji et al., 2014).

However, questions may arise from comparing parameters measured on samples and LWD data acquired *in situ*, in particular at the bottom of the drilled section. Kitajima et al. (2017) already remarked that porosity continues decreasing below ~2,000 mbsf, while *P* wave velocity data from LWD remain constant or decrease slightly with depth. They interpreted the absence of a V_p trend as evidence of moderate overpressuring. Alternatively, an increase in fracture intensity could cause scale effects even in the absence of overpressuring. Our study further shows that variations in clay-bound water content cannot help explaining why, in this interval, sample porosity decreases while LWD V_p remains constant. All these observations indicate that the *in situ* porosity trend deviates from the sample porosity trend at the bottom of the borehole. This may indicate that some overpressuring, occurring postconsolidation, is indeed present. Smectite–illite transformation (Figure 1) in a low-permeability formation could be a factor for in situ pore pressure rise. Additional information, like in situ porosity estimates or direct hydraulic measurements, are needed to fully conclude, but this study shows the potential for an accurate estimation of effective porosity and its impacts on petrophysical values to better understand hydromechanics of subduction zones.

Data Availability Statement

Shipboard sample data (lithology, mineralogy, and total porosity) used in this study are available in Kinoshita et al. (2009a), Strasser et al. (2014), Tobin et al. (2015), and Kitajima et al. (2020). Shipboard sonic data are available at https://mlp.ldeo.columbia.edu/logdb/scientific_ocean_drilling/. CEC, effective porosity, clay-bound water content, mercury injection data, modeled V_p, V_s, and effective porosity profiles are available in the OTELo Research Data Repository, accessible through the following link: https://doi.org/10.24396/ORDAR-106.

Acknowledgments
We are very grateful to the expertise and moral support of Expedition 358 Scientists. We thank the editor and the three anonymous reviewers for their suggestions that helped improving the manuscript. We thank IODP France for its support of the petrophysical and CEC analyses. We also thank Hiroko Kitajima for fruitful discussions. Mai-Linh Doan (ISTerre) is part of Labex OSUG@2020 (ANR10 LABX56).

References

Araki, E., Saffer, D. M., Kopf, A. J., Wallace, L. M., Kimura, T., Machida, Y., et al. (2017). Recurring and triggered slow-slip events near the trench at the Nankai Trough subduction megathrust. *Science*, *356*(6343), 1157–1160. https://doi.org/10.1126/science.aan3120

Athy, L. F. (1930). Density, porosity, and compaction of sedimentary rocks. *AAPG Bulletin*, *14*(1), 1–24. https://doi.org/10.1306/3D93289E-16B1-11D7-8645000102C1865D

Bangs, N. L., Hornbach, M. J., Moore, G. F., & Park, J. O. (2010). Massive methane release triggered by seafloor erosion offshore southwestern Japan. *Geology*, *38*(11), 1019–1022. https://doi.org/10.1130/G31491.1

Blum, P. (1997). *Physical properties handbook: A guide to the shipboard measurement of physical properties of deep-sea cores*. Ocean Drilling Program. https://doi.org/10.2973/odp.tn.26.1997

Brie, A., Pampuri, F., Marsala, A., & Meazza, O. (1995). Shear sonic interpretation in bas-bearing sands. In *SPE annual technical conference and exhibition* (pp. 701–713). https://doi.org/10.2523/30595-ms

Brown, K., & Ransom, B. (1996). Porosity corrections for smectite-rich sediments: Impact on studies of compaction, fluid generation and tectonic history. *Geology*, *9*(24), 843–846. https://doi.org/10.1130/0091-7613(1996)024

Castagna, J. P., Batzle, M. L., & Eastwood, R. L. (1985). Relationships between compressional and shear-wave velocities in clastic silicate rocks. *Geophysics*, *50*(4), 571–581. https://doi.org/10.1190/1.1441933

Chhun, C., Kioka, A., Jia, J., & Tsuji, T. (2018). Characterization of hydrate and gas reservoirs in plate convergent margin by applying rock physics to high-resolution seismic velocity model. *Marine and Petroleum Geology*, *92*, 719–732. https://doi.org/10.1016/j.marpetgeo.2017.12.002

Chhun, C., & Tsuji, T. (2021). Pore pressure and gas saturation distribution in the forearc basin of the Nankai subduction zone inferred from high-resolution *Vp* and *Vs*. *Journal of Petroleum Science and Engineering*, *205*, 108911. https://doi.org/10.1016/j.petrol.2021.108911

Conin, M., Henry, P., Bourlange, S., Raimbourg, H., & Reuschlé, T. (2012). Interpretation of porosity and LWD resistivity from the Nankai accretionary wedge in light of clay physicochemical properties: Evidence for erosion and local overpressuring. *Geochemistry, Geophysics, Geosystems*, *12*, Q0AD07. https://doi.org/10.1029/2010GC003381

Doan, M. L., Conin, M., Henry, P., Wiersberg, T., Boutt, D., Buchs, D., et al. (2011). Quantification of free gas in the Kumano fore-arc basin detected from borehole physical properties: IODP NanTroSEIZE drilling Site C0009. *Geochemistry, Geophysics, Geosystems*, *12*, Q0AD06. https://doi.org/10.1029/2010GC003284

Dugan, B. (2015). Data report: Porosity and pore size characteristics of sediments from Site C0002 of the Nankai Trough determined by mercury injection. In M. Strasser, (Eds.), *Proceedings of the Integrated Ocean Drilling Program* (Vol. 338, p. 8). https://doi.org/10.2204/iodp.proc.338.202.2015

Dutilleul, J., Bourlange, S., Conin, M., & Géraud, Y. (2020). Quantification of bound water content, interstitial porosity and fracture porosity in the sediments entering the North Sumatra subduction zone from cation exchange capacity and IODP Expedition 362 resistivity data. *Marine and Petroleum Geology*, *111*, 156–165. https://doi.org/10.1016/j.marpetgeo.2019.08.007

Dutilleul, J., Bourlange, S., & Géraud, Y. (2021). Porosity and compaction state at the active Pāpaku thrust fault in the frontal accretionary wedge of the north Hikurangi margin. *Geochemistry, Geophysics, Geosystems*, *22*, e2020GC009325. https://doi.org/10.1029/2020GC009325

Dutilleul, J., Bourlange, S., Géraud, Y., & Reuschlé, T. (2021). Porosity and permeability evolution in the Tuaheni landslide complex at Hikurangi margin from IODP Sites U1517 and U1519. *New Zealand Journal of Geology and Geophysics*, *1*, 1–19. https://doi.org/10.1080/00288306.2021.1990088

Dutilleul, J., Bourlange, S., Géraud, Y., & Stemmelen, D. (2020). Porosity, pore structure, and fluid distribution in the sediments entering the northern Hikurangi margin, New Zealand. *Journal of Geophysical Research: Solid Earth*, *125*, e2020JB020330. https://doi.org/10.1029/2020JB020330

Erickson, S. N., & Jarrard, R. D. (1998). Velocity–porosity relationships for water-saturated siliciclastic sediments. *Journal of Geophysical Research*, *103*(B12), 30385–30406. https://doi.org/10.1029/98JB02128

Guo, J., & Underwood, M. B. (2012). Data report: Clay mineral assemblages from the Nankai Trough accretionary prism and the Kumano Basin, IODP Expeditions 315 and 316, NanTroSEIZE Stage 1. In K. Kinoshita, & The Expedition 314/315/316 (Eds.), *Proceedings of the Integrated Ocean Drilling Program* (Vol. 314/315/31, p. 45). https://doi.org/10.2204/iodp.proc.314315316.202.2012

Henry, P. (1997). Relationship between porosity, electrical conductivity, and cation exchange capacity in Barbados wedge sediments. In T. Shipley, Y. Ogawa, P. Blum, & J. Bahr (Eds.), *Proceedings of the Ocean Drilling Program, Scientific Results* (Vol. 156). https://doi.org/10.2973/odp.proc.sr.156.020.1997

Henry, P., & Bourlange, S. (2004). Smectite and fluid budget at Nankai ODP sites derived from cation exchange capacity. *Earth and Planetary Science Letters*, *219*(1–2), 129–145. https://doi.org/10.1016/S0012-821X(03)00694-0

Hoffman, N. W., & Tobin, H. J. (2004). An empirical relationship between velocity and porosity for underthrust sediments in the Nankai Trough accretionary prism. In H. Mikada, G. F. Moore, A. Taira, K. Becker, J. C. Moore, & A. Klaus (Eds.), *Proceedings of the Ocean Drilling Program, Scientific Results, 190/196* (Vol. 190, pp. 1–23).

Hunze, S., & Wonik, T. (2007). Compaction in the Nankai and Barbados accretionary prisms: New insights from logging-while-drilling data. *Geochemistry, Geophysics, Geosystems*, *8*, Q02003. https://doi.org/10.1029/2006GC001277

Jeppson, T. N., & Kitajima, H. (2022). Velocity–porosity relations in carbonate and siliciclastic subduction zone input materials. *Geochemistry, Geophysics, Geosystems*, *23*, e2021GC010074. https://doi.org/10.1029/2021GC010074

Katz, A. J., & Thompson, A. H. (1986). Quantitative prediction of permeability in porous rock. *Physical Review B*, *34*(11), 8179–8181. https://doi.org/10.1103/physrevb.34.8179

Katz, A. J., & Thompson, A. H. (1987). Prediction of rock electrical conductivity from mercury injection measurements. *Journal of Geophysical Research*, *92*(B1), 599–607. https://doi.org/10.1029/JB092iB01p00599

Kinoshita, M., Tobin, H., Ashi, J., Kimura, G., Lallemant, S., Screaton, E., & The Expedition 314/315/316 Scientists. (2009a). Expedition 314 Site C0002. In *Proceedings of the Integrated Ocean Drilling Program* (Vol. 314, p. 77). https://doi.org/10.2204/iodp.proc.314315316.114.2009

Kinoshita, M., Tobin, H., Ashi, J., Kimura, G., Lallemant, S., Screaton, E., & The Expedition 314/315/316 Scientists. (2009b). Expedition 315 Site C0002. In *Proceedings of the Integrated Ocean Drilling Program* (Vol. 315, p. 76). https://doi.org/10.2204/iodp.proc.314315316.124.2009

Kitajima, H., Hirose, T., Ikari, M., Kanagawa, K., Kimura, G., Kinoshita, M., et al. (2020). Site C0002. In *Proceedings of the International Ocean Discovery Program* (Vol. 358). https://doi.org/10.14379/iodp.proc.358.103.2020

Kitajima, H., Saffer, D., Sone, H., Tobin, H., & Hirose, T. (2017). In situ stress and pore pressure in the deep interior of the Nankai accretionary prism, Integrated Ocean Drilling Program Site C0002. *Geophysical Research Letters*, *44*, 9644–9652. https://doi.org/10.1002/2017GL075127

Kitajima, H., & Saffer, D. M. (2012). Elevated pore pressure and anomalously low stress in regions of low frequency earthquakes along the Nankai Trough subduction megathrust. *Geophysical Research Letters*, *39*, L23301. https://doi.org/10.1029/2012GL053793

Kitamura, M., Hirose, T., & Lei, X. (2021). Mechanical weakness of the Nankai accretionary prism: Insights from V_p measurements of drill cuttings. *Geochemistry, Geophysics, Geosystems*, *22*, e2020GC009536. https://doi.org/10.1029/2020GC009536

Kominz, M. A., Patterson, K., & Odette, D. (2011). Lithology dependence of porosity in slope and deep marine sediments. *Journal of Sedimentary Research*, *81*(10), 730–742. https://doi.org/10.2110/jsr.2011.60

Miyakawa, A., Saito, S., Yamada, Y., Tomaru, H., Kinoshita, M., & Tsuji, T. (2014). Gas hydrate saturation at Site C0002, IODP Expeditions 314 and 315, in the Kumano Basin, Nankai Trough. *Island Arc*, *23*(2), 142–156. https://doi.org/10.1111/iar.12064

Nur, A., Mavko, G., Dvorkin, J., & Galmudi, D. (1998). "Critical porosity: The key to relating physical properties to porosity in rocks". *The Leading Edge*, *3*, 357–362. https://doi.org/10.1190/1.1437977

Obara, K., & Kato, A. (2016). Connecting slow earthquakes to huge earthquakes. *Science*, *353*(6296), 253–257. https://doi.org/10.1126/science.aaf1512

Orsini, L., & Rémy, J.-C. (1976). Utilisation du chlorure de cobalti-hexamine pour la détermination simultanée de la capacité d'echange et des bases échangeables des sols. *Science du Sol*, *4*, 269–275.

Park, J.-O., Fujie, G., Wijerathne, L., Hori, T., Kodaira, S., Fukao, Y., et al. (2010). A low-velocity zone with weak reflectivity along the Nankai subduction zone. *Geology*, *38*(3), 283–286. https://doi.org/10.1130/G30205.1

Park, J.-O., Tsuru, T., Kodaira, S., Cummins, P. R., & Kaneda, Y. (2002). Splay fault branching along the Nankai subduction zone. *Science*, *297*(5584), 1157–1160. https://doi.org/10.1126/science.1074111

Raimbourg, H., Hamano, Y., Saito, S., Kinoshita, M., & Kopf, A. J. (2011). Acoustic and mechanical properties of Nankai accretionary prism core samples. *Geochemistry, Geophysics, Geosystems*, *12*, Q0AD10. https://doi.org/10.1029/2010GC003169

Saito, S., & Goldberg, D. (1997). Evolution of tectonic compaction in the Barbados accretionary prism: Estimates from logging-while-drilling. *Earth and Planetary Science Letters*, *148*(3), 423–432. https://doi.org/10.1016/S0012-821X(97)00056-3

Saito, S., Miyakawa, A., Yamada, Y., & Kinoshita, M. (2010). Methane hydrate occurrence estimated from downhole logging at IODP Site C0002, Kumano Basin. *Journal of the Japanese Association of Petroleum Technology*, *75*(1), 54–58. https://doi.org/10.3720/japt.75.54

Song, C., & Underwood, M. (2017). Data report: Permeability and microfabric of core samples from IODP Expedition 348, Hole C0002P, Nankai Trough accretionary prism. In H.Tobin, T. Hirose, D. Saffer, S. Toczko, L. Maeda, Y. Kubo, & The Expedition 348 Scientists (Eds.), *Proceedings of the Integrated Ocean Drilling Program* (Vol. 348). https://doi.org/10.2204/iodp.proc.348.201.2017

Strasser, M., Dugan, B., Kanagawa, K., Moore, G., Toczko, S., Maeda, L., et al. (2014). Site C0002. In IODP (Ed.), *Proceedings of the International Ocean Discovery Program* (Vol. 338, p. 248). IODP. https://doi.org/10.2204/iodp.proc.338.103.2014

Tobin, H., Hirose, T., Saffer, D., Toczko, S., Maeda, L., Kubo, Y., et al. (2015). Expedition 348 summary. In IODP (Ed.), *Proceedings of the International Ocean Discovery Program* (Vol. 348). https://doi.org/10.2204/iodp.proc.348.101.2015

Tobin, H., Hirose, T., Ikari, M., Kanagawa, K., Kimura, G., Kinoshita, M. (Eds.), et al. (2020). *Volume 358: NanTroSEIZE plate boundary Deep Riser 4: Nankai seismogenic/slow slip megathrust*. International Ocean Discovery Program. https://doi.org/10.14379/iodp.proc.358.2020

Tosaya, C. A. (1982). *Acoustical properties of clay-bearing rocks* (Unpublished doctoral dissertation). Stanford University.

Tsuji, T., Kamei, R., & Pratt, R. G. (2014). Pore pressure distribution of a mega-splay fault system in the Nankai Trough subduction zone: Insight into up-dip extent of the seismogenic zone. *Earth and Planetary Science Letters*, *396*, 165–178. https://doi.org/10.1016/j.epsl.2014.04.011

Tudge, J., & Tobin, H. J. (2013). Velocity–porosity relationships in smectite-rich sediments: Shikoku Basin, Japan. *Geochemistry, Geophysics, Geosystems*, *14*, 5194–5207. https://doi.org/10.1002/2013GC004974

Underwood, M. B. (2017). Data report: Clay mineral assemblages and illite/smectite diagenesis in cuttings from Hole C0002P, IODP Expedition 348, Nankai Trough accretionary prism. In H. Tobin (Ed.), *Proceedings of the Integrated Ocean Drilling Program* (Vol. 348). https://doi.org/10.2204/iodp.proc.348.204.2017

Underwood, M. B., & Song, C. (2016). Data report: Clay mineral assemblages in cuttings from Hole C0002F, IODP Expedition 338, upper Nankai Trough accretionary prism. In M. Strasser (Ed.), *Proceedings of the Integrated Ocean Drilling Program* (Vol. 338). https://doi.org/10.2204/iodp.proc.338.206.2016

Westbrook, G. K., Chand, S., Rossi, G., Long, C., Bünz, S., Camerlenghi, A., et al. (2008). Estimation of gas hydrate concentration from multi-component seismic data at sites on the continental margins of NW Svalbard and the Storegga region of Norway. *Marine and Petroleum Geology*, *25*(8), 744–758. https://doi.org/10.1016/j.marpetgeo.2008.02.003